nature materials

Article

https://doi.org/10.1038/s41563-023-01595-0

Operando electron microscopy investigation of polar domain dynamics in twisted van der Waals homobilayers

Received: 22 March 2022

Accepted: 30 May 2023

Published online: 26 June 2023

Check for updates

Kahyun Ko[1,10], Ayoung Yuk[1,10], Rebecca Engelke[2,10], Stephen Carr[2,3], Junhyung Kim[1], Daesung Park[1], Hoseok Heo[2,4], Hyun-Mi Kim[5], Seul-Gi Kim[5], Hyeongkeun Kim[5], Takashi Taniguchi[6], Kenji Watanabe[7], Hongkun Park[2,4], Efthimios Kaxiras[2,8], Sang Mo Yang[1] ✉, Philip Kim[2,8] ✉ & Hyobin Yoo[1,9] ✉

Conventional antiferroelectric materials with atomic-scale anti-aligned dipoles undergo a transition to a ferroelectric (FE) phase under strong electric fields. The moiré superlattice formed in the twisted stacks of van der Waals crystals exhibits polar domains alternating in moiré length with anti-aligned dipoles. In this moiré domain antiferroelectic (MDAF) arrangement, the distribution of electric dipoles is distinguished from that of two-dimensional FEs, suggesting dissimilar domain dynamics. Here we performed an operando transmission electron microscopy investigation on twisted bilayer WSe_2 to observe the polar domain dynamics in real time. We find that the topological protection, provided by the domain wall network, prevents the MDAF-to-FE transition. As one decreases the twist angle, however, this transition occurs as the domain wall network disappears. Exploiting stroboscopic operando transmission electron microscopy on the FE phase, we measure a maximum domain wall velocity of 300 μm s^{-1}. Domain wall pinnings by various disorders limit the domain wall velocity and cause Barkhausen noises in the polarization hysteresis loop. Atomic-scale analysis of the pinning disorders provides structural insight on how to improve the switching speed of van der Waals FEs.

In two-dimensional (2D) heterostructures, a desired crystal symmetry can be engineered by controlling the stacking angle between two layers[1]. Starting from the 2D building block of monolayer transition metal dichalcogenides (TMDs) with trigonal prismatic coordination (point group D_{3h}), one can fabricate an artificial bilayer that has either a non-centrosymmetric polar structure (point group C_{3v}) or a centrosymmetric non-polar structure (point group D_{3d}) by controlling the stacking angle (Supplementary Section 1.1). In the untwisted TMD bilayer without inversion symmetry (Fig. 1a), electric charges can transfer from one layer to the other, thereby exhibiting spontaneous polarization in the out-of-plane direction[2–9]. Depending on the in-plane shifting direction between the two layers, the charge transfers

[1]Department of Physics, Sogang University, Seoul, Republic of Korea. [2]Department of Physics, Harvard University, Cambridge, MA, USA. [3]Department of Physics, Brown University, Providence, RI, USA. [4]Department of Chemistry and Chemical Biology, Harvard University, Cambridge, MA, USA. [5]Korea Electronics Technolgy Institute, Seongnam, Republic of Korea. [6]International Center for Materials Nanoarchitectonics, National Institute for Materials Science, Tsukuba, Japan. [7]Research Center for Functional Materials, National Institute for Materials Science, Tsukuba, Japan. [8]John A. Paulson School of Engineering and Applied Sciences, Harvard University, Cambridge, MA, USA. [9]Institute of Emergent Materials, Sogang University, Seoul, Republic of Korea. [10]These authors contributed equally: Kahyun Ko, Ayoung Yuk, Rebecca Engelke. ✉e-mail: smyang@sogang.ac.kr; pkim@physics.harvard.edu; hyobinyoo@sogang.ac.kr

https://doi.org/10.1038/s41563-023-01595-0

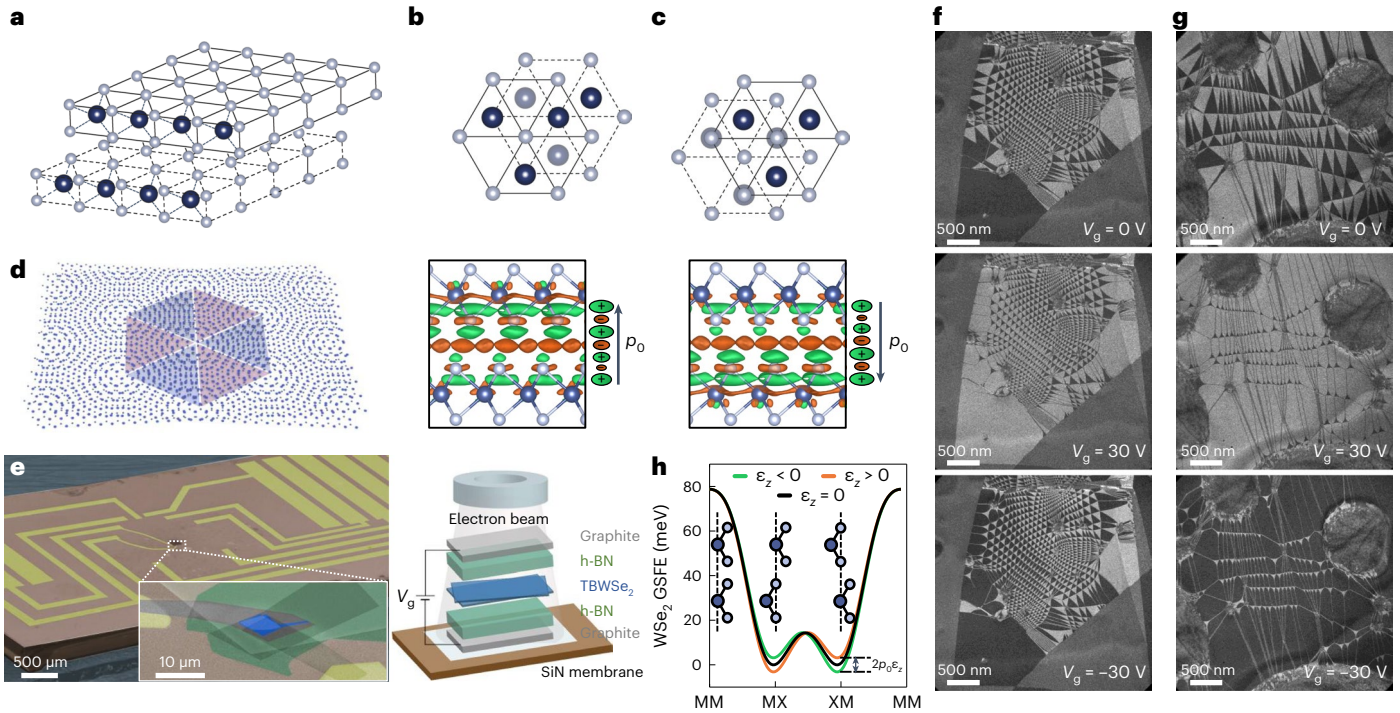

Fig. 1 | Operando TEM investigation of domain dynamics in twisted bilayer TMDs. a, Schematic diagram in perspective view of a parallel-aligned bilayer TMD to induce a dipole moment in the out-of-plane direction. **b**,**c**, Schematic diagrams of bilayer TMD in a top view (top) and side view (bottom) with their corresponding charge distributions. The directions of in-plane lattice shifts are opposite to develop the up polarization in the MX configuration (**b**) and down polarization in the XM configuration (**c**). The bottom panels show the density functional theory calculation of positive (green) and negative (orange) charge distribution, where p_0 is the average dipole moment per atomic unit cell pointing in opposite directions for the MX (**b**) and the XM (**c**) stacking configurations. **d**, Schematic diagram of twisted bilayer TMD where the alternating triangular MX and XM domains are formed as a result of atomic reconstruction at the interface. **e**, Colour-coded scanning electron microscopy image (left) and schematic diagram (right) of operando TEM device fabricated on thin membrane for real-time observation of domain dynamics. Graphite and h-BN layers act as an electron-beam-transparent gate electrode and insulating layer, respectively. V_g, gate voltage. **f**,**g**, DF TEM images ($g = 10\bar{1}0$) of twisted bilayer TMD taken at three different gate voltage conditions (Supplementary Videos 1 and 2 for real-time observations of structural change as a function of gate voltage in the same regions). **h**, Computed generalized stacking-fault energy (GSFE) with (orange and green curves) and without (black curve) an electric field.

in opposite directions, which results in the up (down) polarization in the MX (XM) configuration (Fig. 1b,c), where M and X represent the metal and chalcogen atoms, respectively. In the twisted bilayer TMD, with a small twist angle relative to the parallel stacking, periodic lattice modulation along with the moiré superlattice yields an array of triangular MX and XM domains (Fig. 1d)[5–14]. Here the opposite directions of the vertical polarizations in the MX and XM domains alternate in a moiré length scale, which is distinguished from the polarization distribution in the recently reported 2D ferroelectrics[8,15,16]. According to previous reports[9,13], the domain structure changes under an electric field, but the correlation of such domain structural change with the FE hysteresis has not been fully understood. Furthermore, these recent reports are based on piezoresponse force microscopy and scanning electron microscopy with limited temporal resolution, lacking real-time information of the domain wall motion that governs the domain dynamics.

We developed an operando transmission electron microscopy (TEM) platform to investigate the polar domain dynamics under an electric field with unprecedented spatial and temporal resolution. Thin graphite and hexagonal boron nitride (h-BN) layers are exploited as metallic and insulating components of the device (Fig. 1e and Supplementary Section 1.2). Since these van der Waals (vdW) stacking layers exhibit single-crystalline diffraction patterns, we can readily filter out their diffraction in Fourier space. Therefore, the graphite and h-BN layers serve as electron-beam-filterable gates and gate dielectrics on the operando TEM platform, allowing us to perform dark-field (DF) TEM imaging on the buried twisted TMD interfaces. In this operando TEM device structure, a temporal resolution of 200 ms in real-time imaging was achieved, which can be further improved by optimizing the DF imaging condition or modifying the device structure. Figure 1f,g shows DF TEM images taken with the $g = 10\bar{1}0$ Bragg peak of the TMD. Bright and dark contrasts in the images represent MX and XM domains, respectively[3,17,18]. Upon applying a positive (negative) top gate voltage onto the dual-gated devices, the MX domains increase (decrease) their area, with the opposite behaviour for the XM domains (Supplementary Videos 1 and 2 for real-time observation). The opposite trend in structural changes in the MX and XM domains in response to the gate voltages indicates that the polarizations in MX and XM domains are in opposite directions, as described in Fig. 1b,c.

Moiré domain antiferroelectrics

The structural change is associated with the change in vdW stacking energy under the electric field. The vdW stacking energy plotted as a function of stacking order (black curve in Fig. 1h) indicates that there are two-fold-degenerate structural ground states corresponding to MX and XM stackings at zero electric field[9–11,13]. Due to the two-fold degeneracy, we observe equal portions of MX and XM domains under zero electric field. However, this degeneracy can be lifted via perpendicular electric fields generated by the top and bottom gate voltages. For instance, if the electric field applied by the gate voltages aligns parallel with the polarization direction in MX (XM) domains and antiparallel with the polarization direction in XM (MX) domains, the stacking energy of the MX (XM) domains is lowered compared with that of the XM (MX)

domains, as shown by the orange (green) curve in Fig. 1h. Such changes in the stacking energy landscape serve as the driving force for the structural changes: the domain boundaries move so that the domains with the lower energy configuration dominate over the ones with the higher energy configuration.

We performed a quantitative analysis of the structural change by choosing an order parameter that describes the normalized relative area (A) of the MX and XM domains, $\widetilde{\Delta A} = \frac{A_{MX} - A_{XM}}{A_{MX} + A_{XM}}$. Since the MX and XM domains each exhibit an intrinsic vertical electric polarization equal in magnitude and opposite in direction, the net polarization P is related to the order parameter $\widetilde{\Delta A}$ as

$$P = p_0 \times \widetilde{\Delta A}$$

where p_0 is the intrinsic dipole moment of the MX stacking (Supplementary Section 2.1 for details). The $\widetilde{\Delta A}$ value plotted as a function of out-of-plane electric field ε_z (right panel in Fig. 2a) from the DF TEM data (left panel of Fig. 2a) shows linear behaviour (Supplementary Video 3 for real-time observation). Such a trend indicates a linear dielectric response of the MDAF to the electric field with the corresponding electric polarizability proportional to the slope of $\widetilde{\Delta A}$ with respect to ε_z. Our systematic analysis shows that the electric polarizability can be tuned in a continuous manner by controlling the twist angle θ (Extended Data Fig. 1 and Supplementary Section 2.1 for details). Moreover, the difference in $\widetilde{\Delta A}$ at forward and backward gate sweeps was mostly within a noise level (right panel in Fig. 2a), indicating that the structural hysteresis in the typical MDAF state is minimized, which is clearly distinguished from the FE behaviour. Although we observe hysteretic domain dynamics for the MDAF with larger domains (Supplementary Section 2.2), such hysteresis seems to be associated with the non-equilibrium arrangement of the domain wall network (DWN) due to the domain walls interactions with the pinning sites with various strengths (detailed description of domain wall relaxation in Supplementary Section 2.3).

Topological protection of the domain wall network

One can make an analogy between a MDAF and a conventional antiferroelectric (AFE) in terms of the dielectric response to the small electric field. Both systems show no remnant net polarization at zero electric field and exhibit a non-hysteretic linear response to the small electric field. The only difference is that the polarizations alternate in the atomic length scale[19] for the conventional AFE system while they alternate in the moiré length scale for the MDAF system. Upon applying large electric fields, however, the MDAF behaves in a different manner compared with the conventional AFE system. In the conventional AFE, a large electric field eventually aligns the electric dipoles to the fields, turning the system to a FE. This electric-field-induced AFE-to-FE transition is responsible for the double hysteresis loop in the polarization–electric field relation in the AFE system[20]. In our MDAF system realized in a moiré lattice, on the other hand, the AFE-to-FE transition was not observed (Fig. 2a, Extended Data Fig. 1a–c and Supplementary Fig. 4). Even for the twisted bilayer with a small twist angle that exhibits a large electric polarizability, the adjacent domain walls cannot annihilate to make a single domain, which is in strong contrast to the conventional AFE.

The absence of a MDAF-to-FE transition in the TMD moiré superlattice can be explained by the topological protection[21] of the DWN in the MDAF. We note that the domain walls formed in the reconstructed moiré lattice can be characterized as dislocation lines with Burgers vectors of partial type, $\mathbf{b} = \frac{1}{3} < 10\bar{1}0 >$, describing the shift of the atomic registry from MX (XM) to XM (MX)[22] (Supplementary Section 2.4 for details). Since these dislocation lines are confined in 2D space, they cannot easily avoid each other as in three-dimensional space, forcing the creation of the moiré DWN where the energetically unfavourable MM configurations are formed at the nodes of the DWN. Under a strong electric field, the neighbouring domain walls in the DWN meet together, and the corresponding Burgers vectors for the neighbouring domain walls always add up to the perfect type of $\mathbf{b} = \frac{1}{3} < 11\bar{2}0 >$ rather than cancelling each other to annihilate (Supplementary Section 2.5 for details). This indicates that the DWN cannot be removed from the system with continuous deformation, and thus the DWN in the MDAF is topologically protected. Furthermore, the density of the nodes of the DWN is determined by the moiré length, suggesting that the density of the nodes should be preserved as long as the global twist angle between the two layers is kept constant[23].

Ferroelectrics

Upon decreasing the twist angle θ, the moiré length λ_m increases and becomes comparable to the sample size D_0. Here the regularly spaced nodes of the DWN are pushed out of the sample, resulting in a completely different domain topology. The domain structure shown in Fig. 2b exhibits three domains in the specimen (marked with three green arrows in image 1 in Fig. 2b) with the two domain walls in between. In the absence of DWNs, application of an electric field makes the domain walls move across the specimen, which enables structural switching. Here we observe a step-like change in polarization plotted as a function of applied electric field, which is known as the Barkhausen effect[24,25] (Supplementary Video 4 for real-time observation). Real-time imaging of the Barkhausen effect provides detailed insight on the domain wall pinning behaviour, which will be discussed more in detail in the following text. Although the domain wall motion is not smooth due to the consecutive pinning and depinning by the disorder in the specimen, $\widetilde{\Delta A}$ plotted as a function of ε_z clearly indicates switchable remnant polarizations distinguished from what was observed in the MDAF state discussed previously.

Although domain walls move freely with some temporary pinnings, the value of $\widetilde{\Delta A}$ plotted as a function of ε_z does not reach 1 or −1 (right panel in Fig. 2b), indicating that the structural switching is incomplete. Since there are two domain walls in the specimen, the motion of one domain wall is eventually impeded by the other domain wall (images 3–5 in Fig. 2b; Supplementary Video 4 for the entire process). We sometimes observe almost complete switching between MX ($\widetilde{\Delta A} \approx 1$) and XM ($\widetilde{\Delta A} \approx -1$), as shown in Fig. 2c (Supplementary Video 5 for real-time observation). Upon applying an electric field, the domain wall moves from one edge to the other edge across the entire specimen to switch the net polarization. However, even in this case, we observe a tiny region with opposite polarization due to the repulsion of the domain walls (image 4 in Fig. 2c). Here, the degree of the polarization switching is determined by the distribution of the domain walls in the specimen. The polarization switching occurs by the motion of the domain walls that were already formed, from the beginning. Unlike in the conventional FE thin films, creation of new domains in the middle of oppositely polarized domains was not observed in our uniform gating experiment. As the polarization switching requires a sliding motion of atoms in a confined 2D space, such motion can occur only in a collective manner. The collective sliding of atoms in one direction from the perfect crystalline region would result in a dislocation loop in 2D space. Generating such a dislocation loop costs a higher energy than moving the existing domain walls in terms of switching the polarization. Thus, understanding the confined motion of dislocation lines and their interaction in 2D space is key to understanding the domain dynamics in 2D FEs and MDAFs.

Transition between MDAFs and FEs

One can design a structural topology of a twisted vdW homobilayer that depends on the twist angle to engineer a polar response of the system (Fig. 2d). According to previous work on twisted bilayer graphene, there is an important structural crossover behaviour at the

https://doi.org/10.1038/s41563-023-01595-0

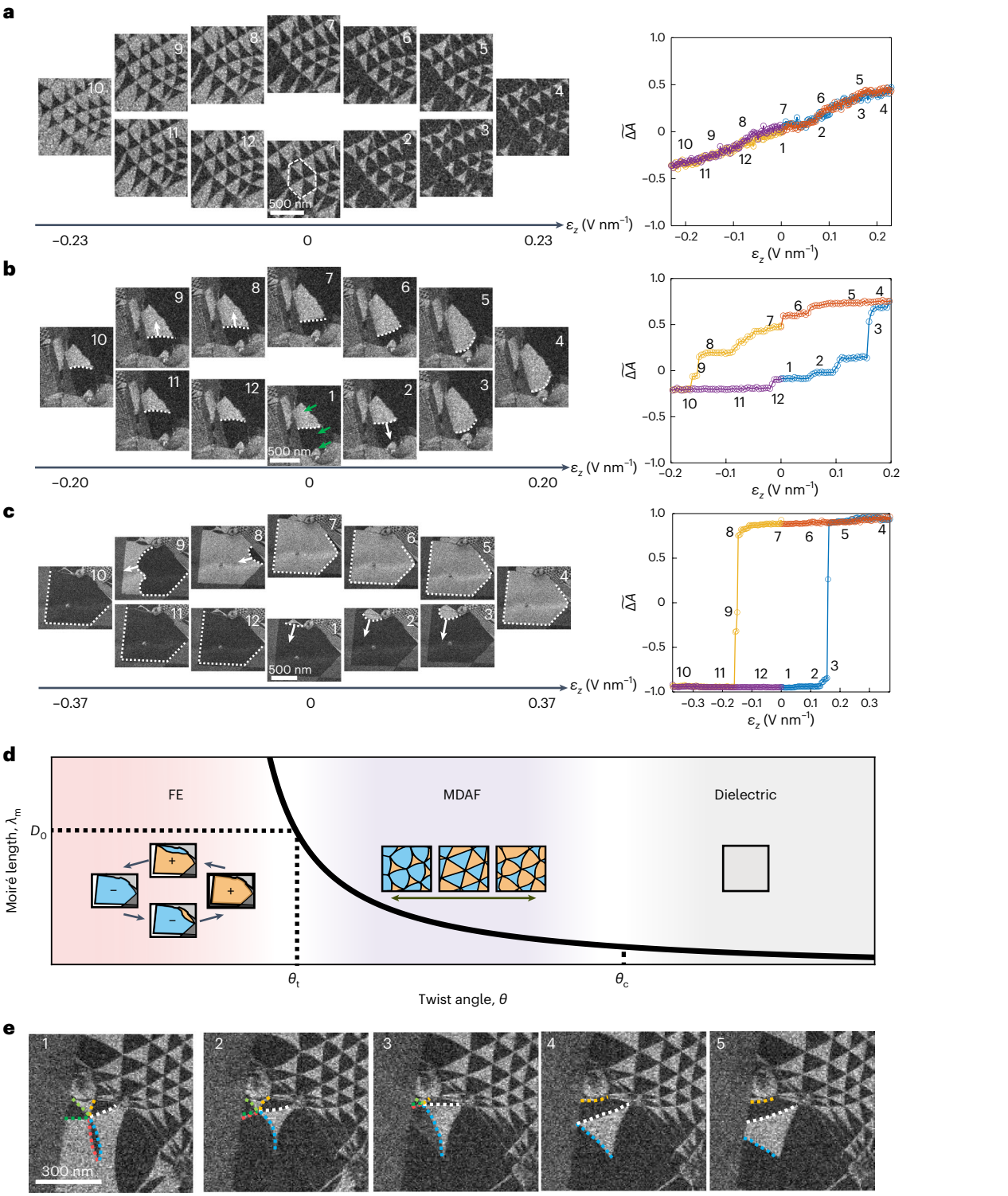

Fig. 2 | MDAF-to-FE transition in twisted bilayer TMD. a–**c**, Snapshots of DF TEM images (g = 10$\bar{1}$0; left) and their corresponding normalized polarization $\widetilde{\Delta A}$ plotted as a function of vertical electric fields during the gate sweeps (Supplementary Videos 3–5 for real-time observation). White dashed line indicates a region where the normalized polarization $\widetilde{\Delta A}$ was estimated. Green arrows in **b** mark the positions of three domains present in the specimen. White dashed lines and arrows in **b** and **c** indicate the domain walls and the directions of domain wall motion, respectively. The numbers marked in the DF images (left) match the corresponding electric fields applied during the sweep, marked with the same numbers in the plots of $\widetilde{\Delta A}$ (right). **d**, Plot of moiré length as a function of twist angle with the schematic representation (inset) of the transition from MDAFs to FEs in the twisted bilayer TMD. **e**, Snapshots of DF TEM images (g = 10$\bar{1}$0) during gate sweeps (Supplementary Video 6 for real-time observation). The node of the DWN (coloured, dashed lines) is pushed out to the sample boundary.

characteristic crossover angle (θ_c)[18]. A vdW twisted bilayer system with a twist angle larger than θ_c ($\theta > \theta_c$) exhibits rotational moiré structures with minimized structural reconstruction. In this regime, the system would exhibit normal dielectric properties at the macroscopic scale, and we do not observe a noticeable structural change upon applying an electric field. Below θ_c, where we clearly observe polar domains,

https://doi.org/10.1038/s41563-023-01595-0

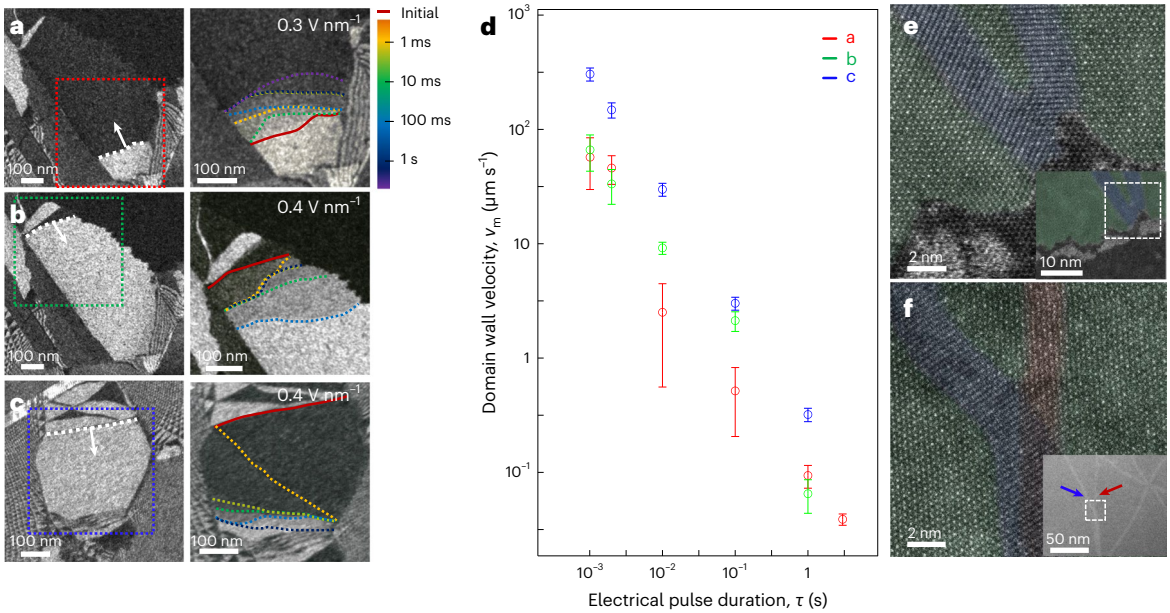

Fig. 3 | FE domain dynamics. a–**c**, DF TEM images (g = 10$\bar{1}$0; left) and the overlay of DF TEM images (right) taken after applying electric pulses with different pulse durations. The DF TEM images in the right panels were taken from the coloured dashed boxes in the left panels in **a**–**c**. The white dashed lines and arrows in the left panels indicate the initial positions of domain walls and their moving directions. Coloured dashed lines in the right panels indicate the position of the domain wall after applying electric pulses, with corresponding pulse widths noted by the colour scale. **d**, Domain wall velocity v_m plotted as a function of electrical pulse duration τ. The red, green and blue data points are taken from the samples shown in **a**, **b** and **c**, respectively. The error bars represent standard deviations of the measured velocities. **e**,**f**, Aberration-corrected ADF STEM images taken at the edge pinning site (**e**) and bulk pinning site (**f**). The green regions indicate MX and XM domains, the blue regions indicate the domain wall and the red region indicates a locally strained region. The insets of **e** and **f** are the lower magnification ADF STEM images. The dashed boxes in the insets indicate the regions where the higher resolution images were taken. The blue and red arrows in the inset of **f** indicate the linear region marked with blue and red colours in **f**.

two distinct domain topologies appear depending on the twist angle. To distinguish the domain topologies, one can count the number of the nodes along the boundary that surrounds a specific domain. In the MDAF arrangement, where one would count the finite number of nodes along the boundary, we observe a non-hysteretic net polarization response. Upon decreasing the twist angle, the moiré length increases until it becomes larger than the sample size, that is, $\lambda_m > D_0$, at the transition angle (θ_t). Below θ_t, the number of nodes found along the boundary becomes 0 as the DWN completely disappears. We observe switchable polar domain dynamics and a clear hysteretic net polarization due to the absence of the DWN obstruction.

One can also manipulate the domain topology to induce the transition from MDAF to FE. When we applied an electric field and monitored the structural change near the edge of the specimen, we could observe that the node of the DWN (coloured dashed lines in Fig. 2e and Extended Data Fig. 2) was pushed out to the sample edge (Supplementary Video 6 for real-time observation). When the node was pushed out to the edge, the domain walls were split, removing the node structure (Fig. 2e). The node never came back once it got pushed out, illustrating that one can engineer the topological configuration of the DWN to induce the MDAF-to-FE transition. Moreover, considering the relation between the density of the nodes in the DWN and the twist angle, the decrease in the local density of the nodes by pushing them out to the edges corresponds to the untwisting of the two TMD layers. Away from the sample edges, bubbles or cracks may act as structural sinks for the nodes. Thus, with the DWN formed inside the perfect crystalline sample, this global untwisting process cannot occur via uniform gating, making the topological protection of MDAF robust in general. However, applying a strong enough electric field in a non-uniform manner by exploiting a local gating configuration might be able to untwist the specimen locally and induce the topological transition between the MDAF state and FE state.

Domain wall dynamics

To further investigate the pinning-driven non-smooth domain wall motion, we exploited operando TEM in a stroboscopic fashion and directly measured the domain wall velocity. For the FE specimen, we located a particular domain wall in the desired initial position (red solid line in the right panels in Fig. 3a–c). Then we applied a pulsed electric field with an incrementally increasing pulse duration and monitored the domain wall position to estimate the domain wall velocity (Fig. 3d), as in stroboscopic piezoresponse force microscopy measurements of the domain wall velocities[26,27]. Note that the initial position of the domain wall is restored between successive pulses so that one can measure the domain wall velocity from the distance the domain wall travels compared to the initial position. The maximum velocity measured in our experiment was ~300 μm s^{-1}, comparable to the domain wall velocity measured in a conventional FE thin film, $PbZr_{0.1}Ti_{0.9}O_3$ (ref. 28). The domain wall velocity v_m was also measured as a function of pulse duration τ (Fig. 3d) from a series of DF images (Fig. 3a–c and Supplementary Section 2.6) taken after applying pulses with different durations. We find that the measured velocity v_m follows a trend ~τ^{-1}, indicating that a few strong pinning centres dominate the domain dynamics. By tracking the positions of the domain wall in τ (coloured dashed lines in the right panels in Fig. 3a–c), we can identify the positions where the domain walls are overlapped closely for different pulse durations. This analysis locates the dominant structural pinning sites that often impede the motion of the dislocation line (domain wall in 2D) on the slip plane.

As noted from the curvature of the domain walls observed in snapshots (Fig. 3a–c), one can see that most common pinning sites exist at the sample edges. Indeed, Barkhausen noises observed in Fig. 2b were mostly related with the edge pinnings. Further detailed analysis indicates that each of the edge pinning sites have different strengths (Supplementary Section 2.7 and Supplementary Video 7 for details). The

pinning sites at the sample edges keep pinning the domain wall in both the forward and backward directions repeatedly in a series of gating experiments (Supplementary Section 2.7 and Supplementary Videos 4 and 7 for details). To investigate the atomistic origin, we also exploited aberration-corrected annular DF (ADF) scanning transmission electron microscopy (STEM) analysis. Although the TMD bilayer specimen seems to show straight edges within the spatial resolution provided by the DF TEM images, aberration-corrected ADF STEM analysis reveals that the edge of the bilayer region shows nanometre-scale roughnesses (Fig. 3e). We found that the domain walls (marked with blue colour in Fig. 3e) are pinned by the region where the edge of the bilayer specimen is intruded or extruded at a nanometre scale (Extended Data Fig. 3 and Supplementary Section 2.8). We believe the interlayer sliding of the bilayer specimen is impeded by the nanometre-scale extrusion or intrusion in the sample edges. This indicates that engineering the cleaner and flatter edge structures in a bilayer specimen might be crucial to enhance the domain wall velocity for a faster switching capability.

We also observed that a domain wall can be pinned in the bulk region inside the domain. Most notably, we observe a pinning of the domain wall due to a structural imperfection such as a bubble (image 9 in Fig. 2c, Extended Data Fig. 4 and Supplementary Videos 5 and 8), which is consistent with previous reports[9,13]. The bubbles are known to be formed by the hydrocarbon that agglomerates in between the top and bottom TMD layers, leading to an incompletely registered region in the TMD bilayer. Therefore the bubbles can be bulk pinning sites for the domain wall motion.

Another type of bulk pinning site that we observed in our experiment is associated with the atomic steps and terraces in the adjacent layers. To identify the atomistic origin for the bulk pinning behaviour, we took the ADF STEM images (Fig. 3f and Extended Data Figs. 5b and 6c) and bright-field STEM images (Extended Data Figs. 5c and 6d) in the region where the domain wall pinning was confirmed (Extended Data Fig. 4a and Supplementary Section 2.8). In the ADF STEM image shown in Fig. 3f, we find that the domain wall is pinned at the junction where the domain wall (marked with blue in Fig. 3f) and another linear feature (marked with red in Fig. 3f) split from each other. Further detailed TEM analysis (Supplementary Section 2.8) indicates that the red-marked linear feature in Fig. 3f corresponds to the locally strained region of the TMD bilayer originating from the step and terrace structure in the adjacent h-BN layer. This suggests that the disorders in the neighbouring layers can be another source for the domain wall pinning event.

By comparing the snapshots of DF TEM images with their corresponding data points in the $\widetilde{\Delta A}$ versus ε_z curve, we conclude that the pinning sites, such as rough edges, bubbles or disorders in the adjacent layer, can all contribute to the Barkhausen noises in the polarization hysteresis curve. Temporary pinning of the domain walls by various structural pinning sites[29] might explain the stochastic variation of the 2D FE switching behaviour reported previously[15]. We also note that the strength of the domain wall pinning sites and their distribution in the specimen will determine the overall domain wall propagation velocity. Our operando TEM analysis suggests that the control of structural disorder in the specimen can enhance the switching speed of vdW FEs for fast-switching device applications.

Online content

Any methods, additional references, Nature Portfolio reporting summaries, source data, extended data, supplementary information, acknowledgements, peer review information; details of author contributions and competing interests; and statements of data and code availability are available at https://doi.org/10.1038/s41563-023-01595-0.

References

1. Du, L. et al. Engineering symmetry breaking in 2D layered materials. *Nat. Rev. Phys.* **3**, 193–206 (2021).
2. Li, L. & Wu, M. Binary compound bilayer and multilayer with vertical polarizations: two-dimensional ferroelectrics, multiferroics, and nanogenerators. *ACS Nano* **11**, 6382–6388 (2017).
3. Sung, J. et al. Broken mirror symmetry in excitonic response of reconstructed domains in twisted $MoSe_2$/$MoSe_2$ bilayers. *Nat. Nanotechnol.* **15**, 750–754 (2020).
4. Ferreira, F., Enaldiev, V. V., Fal'ko, V. I. & Magorrian, S. J. Weak ferroelectric charge transfer in layer-asymmetric bilayers of 2D semiconductors. *Sci. Rep.* **11**, 13422 (2021).
5. Woods, C. et al. Charge-polarized interfacial superlattices in marginally twisted hexagonal boron nitride. *Nat. Commun.* **12**, 347 (2021).
6. Yasuda, K., Wang, X., Watanabe, K., Taniguchi, T. & Jarillo-Herrero, P. Stacking-engineered ferroelectricity in bilayer boron nitride. *Science* **372**, 1458–1462 (2021).
7. Vizner Stern, M. et al. Interfacial ferroelectricity by van der Waals sliding. *Science* **372**, 1462–1466 (2021).
8. Liu, Y., Liu, S., Li, B., Yoo, W. J. & Hone, J. Identifying the transition order in an artificial ferroelectric van der Waals heterostructure. *Nano Lett.* **22**, 1265–1269 (2022).
9. Wang, X. et al. Interfacial ferroelectricity in rhombohedral-stacked bilayer transition metal dichalcogenides. *Nat. Nanotechnol.* **17**, 367–371 (2022).
10. Carr, S. et al. Relaxation and domain formation in incommensurate 2D heterostructures. *Phys. Rev. B* **98**, 224102 (2018).
11. Enaldiev, V., Zólyomi, V., Yelgel, C., Magorrian, S. & Fal'ko, V. Stacking domains and dislocation networks in marginally twisted bilayers of transition metal dichalcogenides. *Phys. Rev. Lett.* **124**, 206101 (2020).
12. Rosenberger, M. R. et al. Twist angle-dependent atomic reconstruction and moiré patterns in transition metal dichalcogenide heterostructures. *ACS Nano* **14**, 4550–4558 (2020).
13. Weston, A. et al. Interfacial ferroelectricity in marginally twisted 2D semiconductors. *Nat. Nanotechnol.* **17**, 390–395 (2022).
14. Weston, A. et al. Atomic reconstruction in twisted bilayers of transition metal dichalcogenides. *Nat. Nanotechnol.* **15**, 592–597 (2020).
15. Fei, Z. et al. Ferroelectric switching of a two-dimensional metal. *Nature* **560**, 336–339 (2018).
16. Liu, F. et al. Room-temperature ferroelectricity in $CuInP_2S_6$ ultrathin flakes. *Nat. Commun.* **7**, 12357 (2016).
17. Brown, L. et al. Twinning and twisting of tri- and bilayer graphene. *Nano Lett.* **12**, 1609–1615 (2012).
18. Yoo, H. et al. Atomic and electronic reconstruction at the van der Waals interface in twisted bilayer graphene. *Nat. Mater.* **18**, 448–453 (2019).
19. Kittel, C. Theory of antiferroelectric crystals. *Phys. Rev.* **82**, 729–732 (1951).
20. Randall, C. A., Fan, Z., Reaney, I., Chen, L. Q. & Trolier-McKinstry, S. Antiferroelectrics: history, fundamentals, crystal chemistry, crystal structures, size effects, and applications. *J. Am. Ceram. Soc.* **104**, 3775–3810 (2021).
21. Huang, F.-T. & Cheong, S.-W. Aperiodic topological order in the domain configurations of functional materials. *Nat. Rev. Mater.* **2**, 17004 (2017).
22. Butz, B. et al. Dislocations in bilayer graphene. *Nature* **505**, 533–537 (2014).
23. Engelke, R. et al. Topological nature of dislocation networks in two-dimensional moiré materials. *Phys. Rev. B* **107**, 125413 (2023).
24. Rudyak, V. M. The Barkhausen effect. *Sov. Phys. Usp.* **13**, 461–479 (1971).

25. Shur, V. Y., Rumyantsev, E., Kuminov, V., Subbotin, A. & Kozhevnikov, V. Barkhausen effect in stepped motion of a plane domain boundary in gadolinium molybdate. *Phys. Solid State* **41**, 269–273 (1999).
26. Gruverman, A. et al. Direct studies of domain switching dynamics in thin film ferroelectric capacitors. *Appl. Phys. Lett.* **87**, 082902 (2005).
27. Yang, S. M. et al. Domain wall motion in epitaxial $Pb(Zr,Ti)O_3$ capacitors investigated by modified piezoresponse force microscopy. *Appl. Phys. Lett.* **92**, 252901 (2008).
28. McGilly, L., Yudin, P., Feigl, L., Tagantsev, A. & Setter, N. Controlling domain wall motion in ferroelectric thin films. *Nat. Nanotechnol.* **10**, 145–150 (2015).
29. Alden, J. S. et al. Strain solitons and topological defects in bilayer graphene. *Proc. Natl Acad. Sci. USA* **110**, 11256–11260 (2013).

Methods

Sample fabrication for TEM experiment

Top graphite and h-BN layers were picked up by an adhesive polymer (poly(bisphenol A carbonate)) stamp-in sequence. Using the stack of the graphite and h-BN layer, a monolayer TMD layer was torn into two pieces and reengaged after controlling the twist angle between the pieces, as reported elsewhere[30,31]. Then the bottom h-BN and graphite layers were picked up one after the other to fabricate the dual-gated twisted bilayer TMD specimen. The whole stack was transferred onto a 50-nm-thick SiN membrane for TEM investigation. Then 10- to 30-nm-thick h-BN and <10-nm-thick graphite were used as the gate dielectric and gate electrode layers, respectively, for DF TEM analysis. The graphite/h-BN/twisted bilayer TMD/graphite heterostructure was suspended on the perforated SiN membrane chips, with the total thickness of the h-BN and graphite layers of less than 3 nm for atomic-resolution structural investigation by aberration-corrected STEM. Using electron-beam lithography and photo lithography, we designed metal electrodes and pads to make an electrical connection to the top and bottom graphite gates. The 5-nm-thick Cr was deposited as an adhesion layer, and 70-nm-thick Au was deposited for the electrical leads and pads.

Operando TEM experiment

Field-emission TEM (Jeol 2010F, Jeol 2100F) with acceleration voltages of 80 kV, 120 kV and 200 kV were used for DF TEM imaging and selected-area electron diffraction. DF TEM imaging ($g = 10\bar{1}0$) was applied to image the MX and XM domains formed in the twisted bilayer TMD. To obtain domain contrast, we tilted the specimens 2–8° in the TEM[17,18]. Selecting the $g = 10\bar{1}0$ peak from the TMD and filtering out other Bragg peaks from h-BN and graphite enables the selective imaging of domains in the TMD, which is buried in between the gate and gate dielectric layers. For the atomic-resolution imaging, spherical aberration-corrected STEM (Jeol ARM 200F) was used with an acceleration voltage of 80 kV. Inner collection and outer collection semi-angles of 54 mrad and 220 mrad were used for ADF STEM imaging. A d.c. sourcemeter (Keithley 2450) was connected to the electrical biasing holder (HennyZ JDCHB-9) to apply a gate voltage onto the dual-gated devices. A high-speed complementary metal oxide semiconductor sensor (Gatan OneView 1095.IS) was used for DF video recording and imaging. Videos were taken with a rate of 5–20 fps. The perpendicular electric field ε_z was computed from the voltage difference V between the top and bottom gates by $\varepsilon_z = V/(\left(\frac{\varepsilon_2}{\varepsilon_1}\right)h_1 + h_2)$ where h_1 is the total thickness of h-BN, $\varepsilon_1 = 3.76$ is the dielectric constant of h-BN, h_2 is the thickness of WSe_2 and $\varepsilon_2 = 7.7$ is the dielectric constant of WSe_2.

Density functional theory calculation

The electronic dipole moment in bilayer WSe_2 was calculated using the Vienna Ab initio Simulation Package with projector augmented-wave Perdew–Burke–Ernzerhof potentials. Our slab calculations used a c-axis height of 30 Å, leaving 20 Å of vacuum between periodic images. For each stacking between the two layers, the vertical position of the atoms was allowed to relax, with a 10^{-5} eV convergence criterion. A 500 eV energy cut-off and a 10^{-8} eV convergence criterion were used for electronic optimization across k points on a $17 \times 17 \times 1$ Γ-centred grid. A minimal mixing parameter for the charge dielectric function of 10 meV was used, as well as a 10 meV energy smearing of electronic energies. To accurately predict the dipole moment, the static ion-clamped dielectric matrix was calculated, and the dipole moment was calculated only for the c axis, out-of-plane of the slab geometry.

Elastic model

The numerical results for a fully elastic model were generated using the method presented in ref. 10. The stacking energy was made dependent on the external variable ε_z, such that the value at MX and XM stacking correctly reproduced the density functional theory results, and the energy at MM stacking was unchanged. Borrowing the notation of stacking-order parameters (v, w) for the 2π unit square from ref. 10, the stacking-fault energy is

$$V_{\mathrm{GSFE}} = c_1[\cos v + \cos w + \cos(v+w)] + c_2[\cos(v+2w) + \cos(v-w) + \cos(2v+w)] + c_3[\cos 2v + \cos 2w + \cos(2v+2w)] + c_4[\sin v + \sin w - \sin(v+w)]$$

with $\{c_1, c_2, c_3\} = \{13.85\ \mathrm{meV}, -2.55\ \mathrm{meV}, -0.92\ \mathrm{meV}\}$ per unit cell, and $c_4 = 0.3849\varepsilon_z p_0$. The strain moduli, extracted from density functional theory as well, were taken as $K = 46{,}323$ meV and $G = 30{,}976$ meV per unit cell. Both a reduction of the model's symmetry assumptions and a non-square mesh size were necessary to consider moiré superlattices with aspect ratios $x_s \neq 1$.

Data availability

The data that support the findings of this study are presented in the paper, Extended Data and Supplementary Information. Any other relevant data are available from the corresponding authors upon request and also available at https://doi.org/10.5281/zenodo.7956290.

References

30. Cao, Y. et al. Superlattice-induced insulating states and valley-protected orbits in twisted bilayer graphene. *Phys. Rev. Lett.* **117**, 116804 (2016).
31. Kim, K. et al. Van der Waals heterostructures with high accuracy rotational alignment. *Nano Lett.* **16**, 1989–1995 (2016).

Acknowledgements

We thank F. Spaepen, J. Mundy and D. Bennett for important discussions. K.K., A.Y., J.K., D.P., S.M.Y. and H.Y. acknowledge the support by the Samsung Research Funding & Incubation Center of Samsung Electronics under project number SRFC-MA2002-01. S.M.Y. and H.Y. acknowledge the support by the National Research Foundation of Korea grant funded by the Korean government (Ministry of Science and ICT; no. 2022R1A4A1033562). P.K. acknowledges the support from the Army Research Office's Multidisciplinary University Initiative (MURI) programme (W911NF-21-2-0147). R.E. acknowledges the support from the National Science Foundation (DMR-1922172) for TEM analysis. K.W. and T.T. acknowledge the support from the Japan Society for the Promotion of Science KAKENHI (grant nos 19H05790, 20H00354 and 21H05233).

Author contributions

H.Y., P.K. and S.M.Y. conceived the experiments. K.K., A.Y., J.K., D.P. and H.Y. fabricated the TEM devices. K.K., A.Y., R.E., J.K., H.-M.K., S.-G.K., H.K. and H.Y. performed the TEM experiments. K.K., A.Y., R.E., S.C., H.-M.K., E.K., S.M.Y., P.K. and H.Y. analysed the data. S.C. performed the theoretical analysis. H.H. and H.P. grew the bulk WSe_2 crystals. K.W. and T.T. grew the bulk h-BN crystals. K.K., A.Y., R.E., S.C., S.M.Y., P.K. and H.Y. wrote the manuscript. All authors contributed to the overall scientific interpretation and edited the manuscript.

Competing interests

The authors declare no competing interests.

Additional information

Extended data is available for this paper at https://doi.org/10.1038/s41563-023-01595-0.

Supplementary information The online version contains supplementary material available at https://doi.org/10.1038/s41563-023-01595-0.

Correspondence and requests for materials should be addressed to Sang Mo Yang, Philip Kim or Hyobin Yoo.

Peer review information *Nature Materials* thanks Moshe Ben Shalom and the other, anonymous, reviewer(s) for their contribution to the peer review of this work.

https://doi.org/10.1038/s41563-023-01595-0

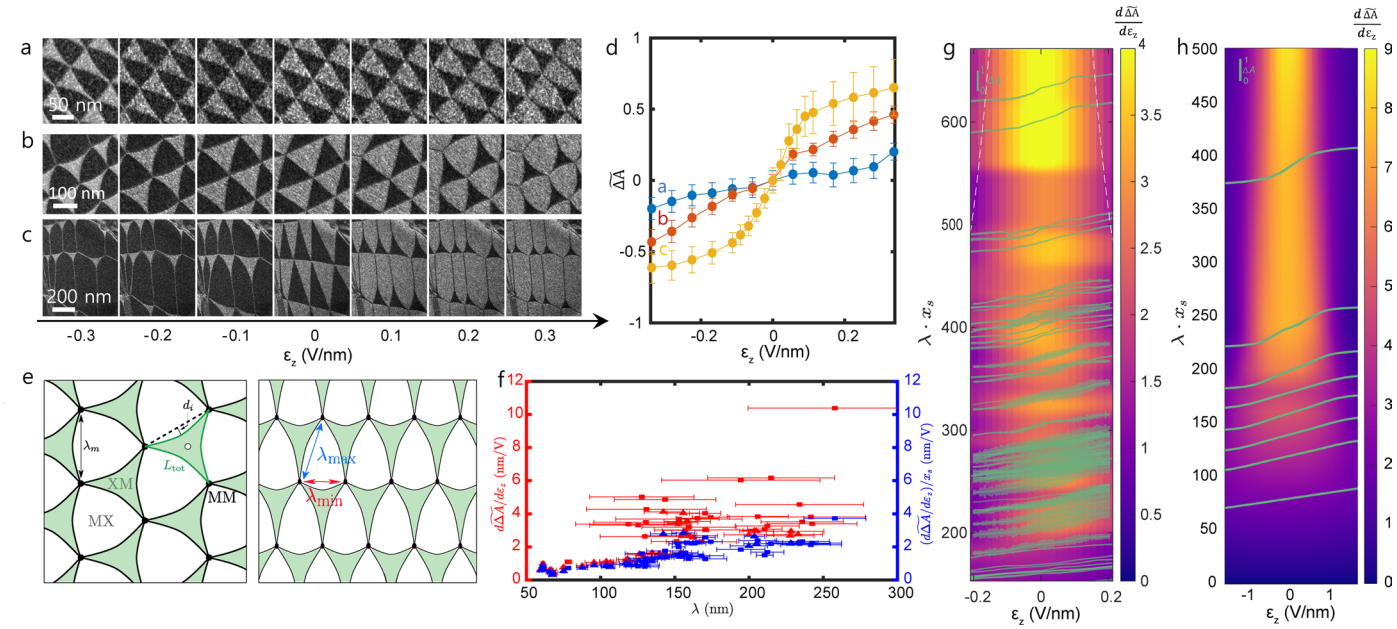

Extended Data Fig. 1 | Tunable polarizability of the twisted bilayer TMD by moiré length and domain anisotropy. (a-c) TEM dark field (DF) images of twisted bilayer TMD plotted as a function of vertical electric field ε_z for different moiré lengths. (d) The normalized domain area difference $\widetilde{\triangle A}$ plotted as a function of ε_z for the three different moiré lengths shown in (a-c). The error bars are a result of the uncertainty in the thresholding operation on the dark and light pixels. (e) Schematics of moiré cell geometry under electric field. When the relative displacement between the top and bottom layer only includes the rotational component, the domain structure shows equilateral triangles (left). When the relative displacement includes the rotational as well as the uniaxial components, the domain structure shows distorted triangular shapes (right). (f) polarizability change with the moiré size and shape. We plot $d\widetilde{\triangle A}/d\varepsilon_z$ (red colour symbols, left axis) and $x_s^{-1} d\widetilde{\triangle A}/d\varepsilon_z$ (blue colour symbols, right axis) obtained from moiré cells shown in Extended Data Fig. 1f as a function of the moiré length λ. Triangle marks represent moiré cells with angles within 30% of the equilateral shape ($x_s \cong 1$). Square marks represent moiré cells that deviate further from the equilateral shape ($x_s \gg 1$). Horizontal error bars represent the standard deviations of the sidelengths of each polygon. (g) Colour plot of $d\widetilde{\triangle A}/d\varepsilon_z$ as a function of ε_z and x_s. Green lines are the values of $\widetilde{\triangle A}$ plotted as a function of the vertical electric field ε_z centered at the corresponding value of λx_s. The errors in estimating $\widetilde{\triangle A}$ due to the uncertainty in the thresholding operation on the dark and light pixels are represented as the thicknesses of the green lines. (h) Simulated colour plot of $d\widetilde{\triangle A}/d\varepsilon_z$ and lines of $\widetilde{\triangle A}$ vs ε_z at various values of λx_s.

https://doi.org/10.1038/s41563-023-01595-0

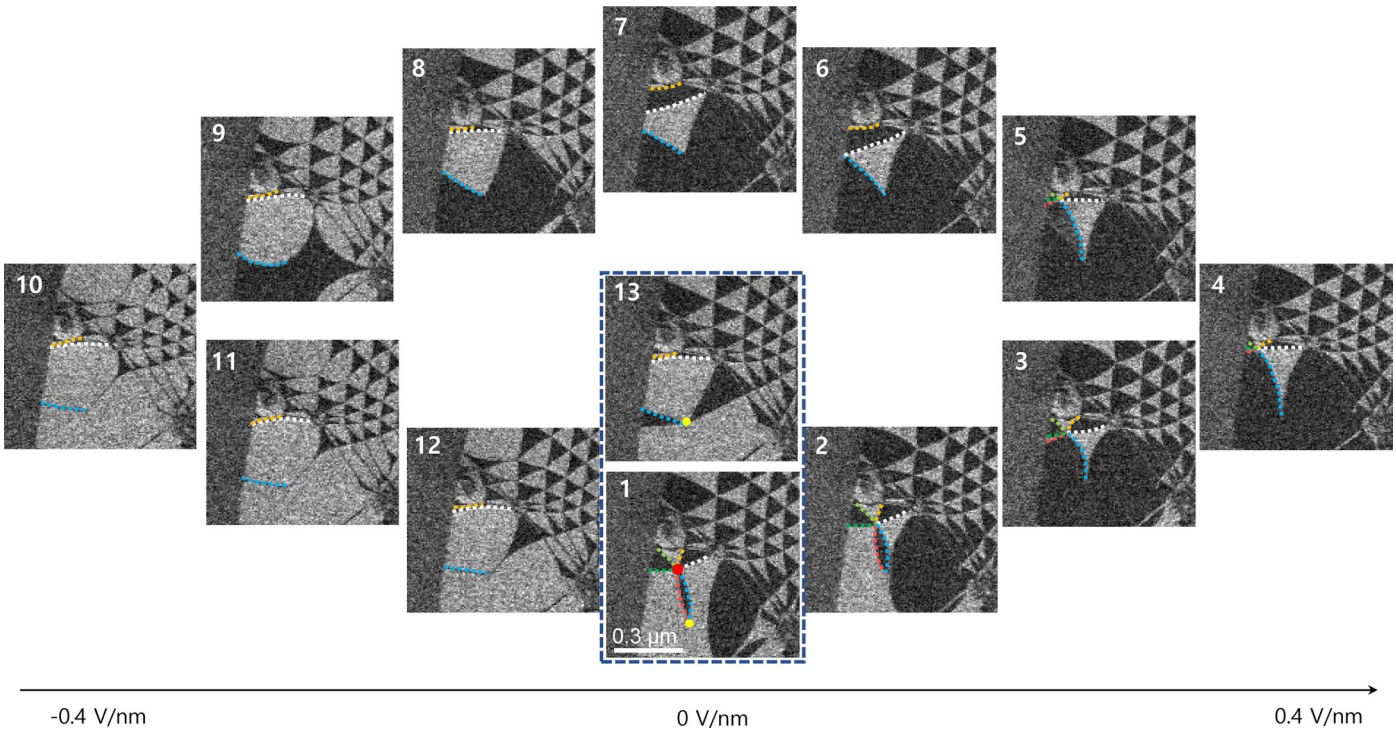

Extended Data Fig. 2 | Removal of the nodes of the DWN at the sample edge. Snapshots of TEM DF images plotted as a function of vertical electric fields during the gate sweep (See Video S6 for real-time observation).

https://doi.org/10.1038/s41563-023-01595-0

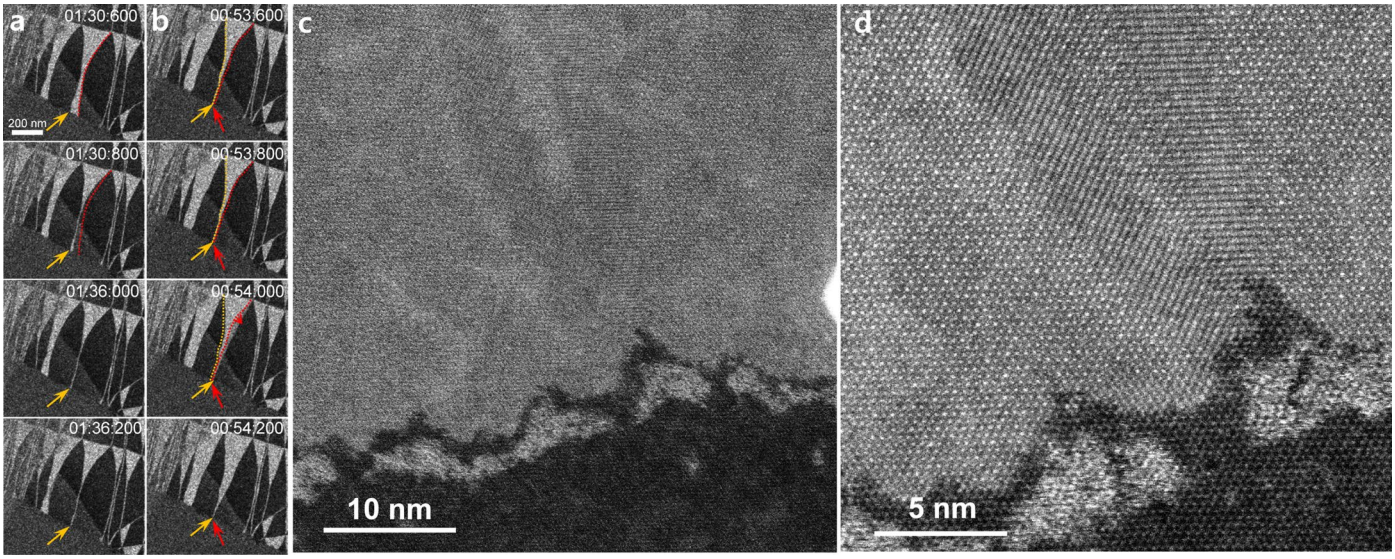

Extended Data Fig. 3 | Domain wall pinning at the sample edge. (a-b) Snap shots of TEM DF images obtained during the electric field sweep. Yellow and red arrows indicate regions where the domain wall is pinned during the electric field sweep. Red and yellow dashed lines are drawn in the same position to show the change in domain wall. (c-d) ADF STEM images taken from the region where the domain wall pinning was confirmed by the snapshots of TEM DF images shown in a and b.

https://doi.org/10.1038/s41563-023-01595-0

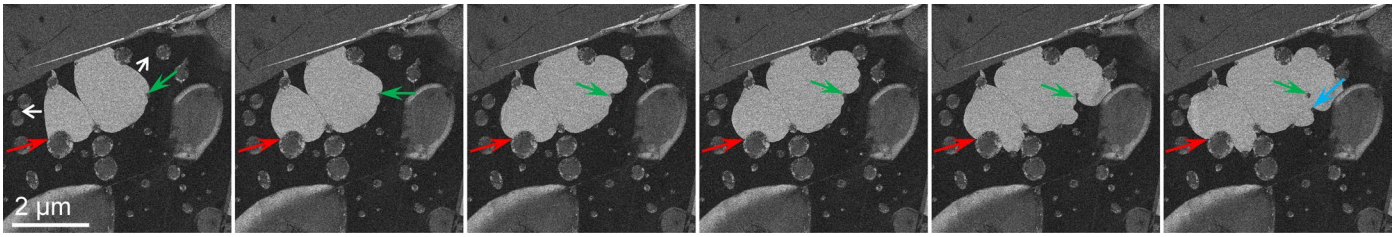

Extended Data Fig. 4 | Domain wall pinning by the bubbles. Snapshots of TEM DF images obtained during the electric field sweep. Coloured arrows indicate some of the pinning events by the bubbles (See Video S8 for real-time observation).

https://doi.org/10.1038/s41563-023-01595-0

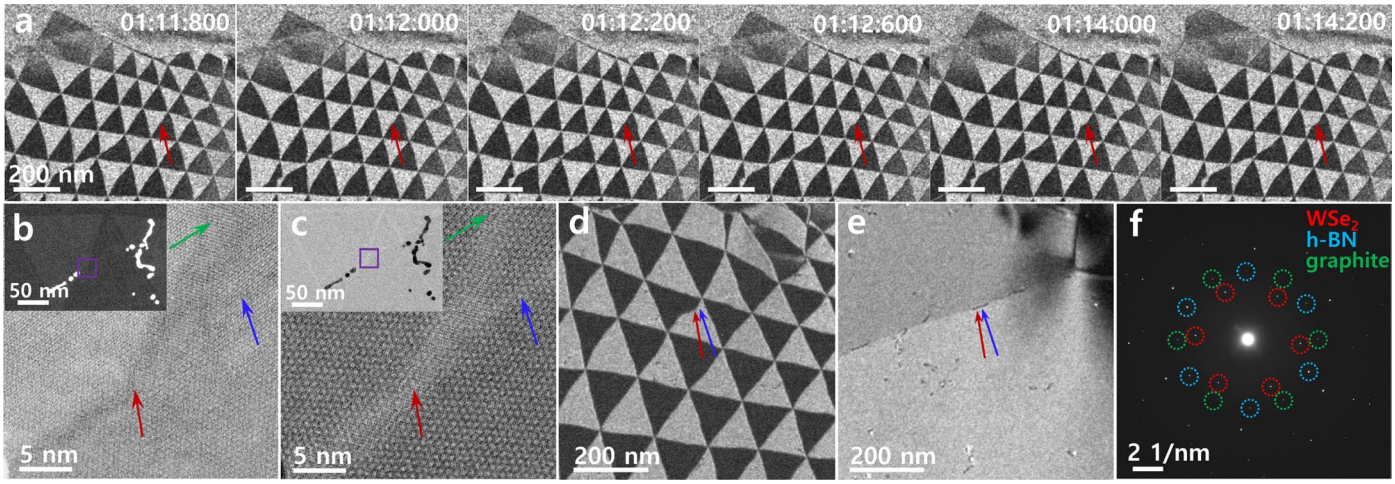

Extended Data Fig. 5 | Domain wall pinning at the bulk pinning sites. (a) Snapshots of TEM DF images obtained during the electric field sweep. The red arrow indicates a region where the domain wall pinning was observed. Magnified (b) ADF and (c) BF STEM images taken in the region where the domain wall pinning was confirmed in (a). The red arrow indicates the curved region in the domain wall caused by the pinning observed in (a). The green arrow indicates the domain wall that extends from the region indicated with the red arrow. The blue arrow indicates the linear feature where the WSe_2 layer is locally strained. The insets show the lower magnification images with the magnified region indicated with the purple boxes. TEM DF images taken with Bragg peaks from WSe_2 (d) and h-BN (e) layers. (f) SAED pattern obtained from the specimen that exhibits the Bragg peaks originating from WSe_2, h-BN, and graphite layers.

https://doi.org/10.1038/s41563-023-01595-0

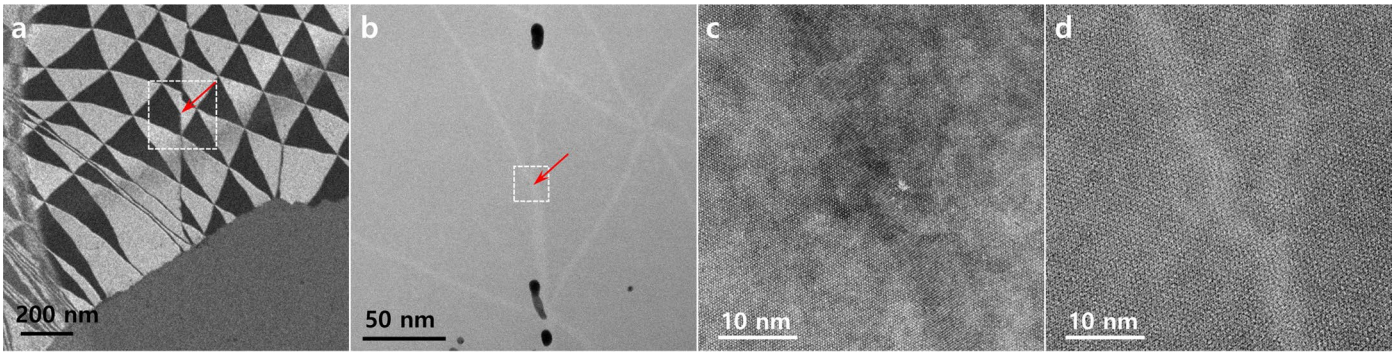

Extended Data Fig. 6 | Domain wall pinning at the bulk pinning sites. (a) TEM DF image obtained from the region where the bulk pinning was confirmed. The red arrow indicates a region where the domain wall pinning was observed. (b) ADF STEM image obtained in the region indicated with the white dashed box in (a). (c) ADF and (d) BF STEM images taken simultaneously in the region marked with the white dashed box in (b).